Nanodiamond-Palladium Core–Shell Organohybrid Synthesis: A Mild Vapor-Phase Procedure Enabling Nanolayering Metal onto Functionalized sp 3 -Carbon

Maria Gunawan, Oana Moncea, Didier Poinsot, Mariem Keskes, Bruno Domenichini, Olivier Heintz, Rémi Chassagnon, Frédéric Herbst, Robert Carlson, Jeremy Dahl, et al.

Nanodiamond-Palladium Core-Shell Organohybrid Synthesis: A Mild Vapor-Phase Procedure Enabling Nanolayering Metal onto Functionalized sp^3-Carbon

*Maria A. Gunawan, Oana Moncea, Didier Poinsot, Mariem Keskes, Bruno Domenichini, Olivier Heintz, Rémi Chassagnon, Frédéric Herbst, Robert M. K. Carlson, Jeremy E. P. Dahl, Andrey A. Fokin, Peter R. Schreiner,*Jean-Cyrille Hierso**

Dr. Maria A. Gunawan, Oana Moncea, Didier Poinsot, Mariem Keskes, Prof. Jean Cyrille Hierso

Institut de Chimie Moléculaire de l'Université de Bourgogne (ICMUB), UMR-CNRS 6302, Université de Bourgogne Franche-Comté, 9 avenue Alain Savary, 21078 Dijon, France

E-mail: jean-cyrille.hierso@u-bourgogne.fr

Dr. Maria A. Gunawan, Oana Moncea, Prof. Andrey A. Fokin, Prof. Peter R. Schreiner

Institut für Organische Chemie, Justus-Liebig-Universität, Heinrich-Buff-Ring 17, 35392 Giessen, Germany

E-mail: prs@uni-giessen.de

Prof. Bruno Domenichini, Dr. Olivier Heintz, Dr. Rémi-Chassagnon, Dr. Frédéric Herbst

Laboratoire Interdisciplinaire Carnot de Bourgogne (ICB), UMR-CNRS 6303, Université de Bourgogne Franche-Comté, 9 avenue Alain Savary, 21078 Dijon, France

Prof. Andrey A. Fokin

Department of Organic Chemistry, Kiev Polytechnic Institute, Pr. Pobedy 37, 03056 Kiev, Ukraine

Prof. Jean Cyrille Hierso

Institut Universitaire de France (IUF), 103 Bd. Saint Michel, 75005 Paris Cedex 5, France

Dr. Jeremy E. P. Dahl, Dr. Robert M. K. Carlson

Stanford Institute for Materials and Energy Sciences, Stanford, CA 94305, USA

Note: M.A.G., O.M., and D.P. contributed equally for this article.

Abstract

We report a novel approach for the bottom-up construction of hybrid organic-inorganic nanocomposites with an intimate arrangement between sp^3-carbon three-dimensional (3D) molecular-size nanodiamonds (diamondoids) and a coated palladium surface as nanolayers. The construction process is conducted stepwisely from the gas phase, using first controlled vapor-phase self-assembly of taylor-made functionalized diamantane derivatives, followed by low-temperature (45 °C) chemical vapor deposition of an organometallic complex (CVD) in a reducing H_2 atmosphere over the self-assembled diamondoid scaffold. The use of self-assemblies of primary diamantane phosphine and phosphine oxide, which are produced with high structural uniformity and reproducibility, yields new hybrid diamondoid-palladium materials incorporating Pd–O–PH–diamantane bonding motifs. Additional investigations provide evidence for a very challenging issue in the intimate construction of sp^3–C/metal scaffolds. SEM and TEM microscopies combined with XPS surface analysis and EDX bulk analysis confirm the formation of diamondoid-palladium organohybrid with unique surface layering. The vapor phase-controlled mild synthetic process allows excellent control over nanocomposite formation and morphology from molecular-level modifications. As such, this bottom-up composite building process bridges scales from the molecular (functionalized diamondoids) over nanoscopic (self-assemblies) to microscopic regime (hybrid), in the challenging association of transition metals with an electronically saturated sp^3-carbon organic host material.

Keywords: diamondoids, nanocomposite, nanodiamonds, nanolayer, palladium, self-assembly, sp^3-C hybrid material

Table of contents graphic

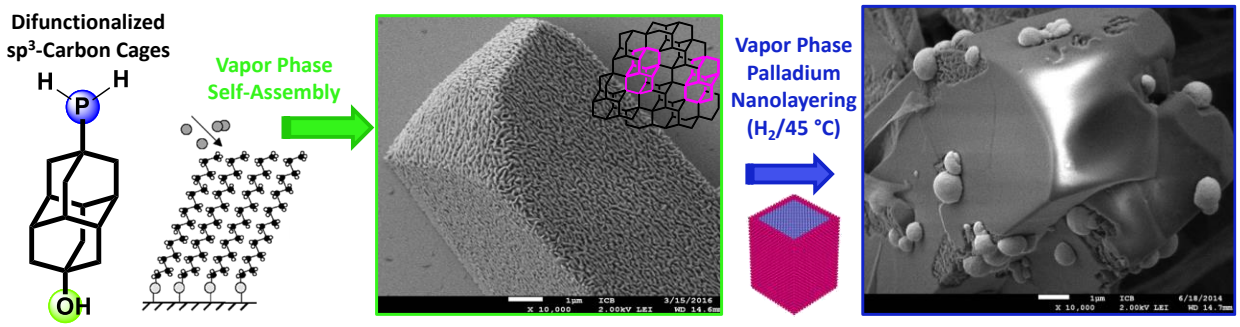

1. Introduction

The rational design and construction of functional materials whose structures are controlled at the nanoscale is a key objective for creating ever smaller devices.[1] Solution- and vapor-phase chemistry have continuously provided advanced methods to synthesize organic[2] and inorganic nanomaterials.[3] In the last decades, research foci have been shifting from single-component to more challenging composite nanoarchitectures.[4] In this respect, metal-carbon surface interactions are at the heart of building nanocomposites. This is well illustrated, for instance, by the intense activity related to metal-organic frameworks (MOFs)[5] or metal-modified graphene materials.[6] Thus, MOF film fabrication progresses through metal-assisted solvothermal solution,[5a, 5b] stepwise liquid epitaxial growth[5b, 7] or vapor-phase construction of hierarchical nanocomposites [metal@MOF]@SAM.[5a] The synthesis of nanocomposites from graphene benefits from the coexistence of aromatic sp^2 domains and functional groups that can be introduced to participate in a wide range of bonding interactions.[8] Those can be conveyed by vapor phase processes[6] as well as solution approaches including hydrothermal transformation[8d, 8e] or co-crystallization.[8f] In all of these cases, structural uniformity and control over morphology is a necessary requirement for realistic applications in nanotechnological devices.

Considering the multiple fundamental and applied aspects of metal/sp^2-carbon based nanocomposites (including fullerenes, CNTs, graphenes, *etc.*),[9] an exciting development in the field of organic-inorganic nanocomposites is the alternative construction of large scale ordered metal/sp^3-carbon based materials. While the synthesis of metal nanocomposites from sp^2-carbon materials benefits from a rich surface chemistry which includes many functional groups, metal/sp^3-carbon based nanostructures are much less developed and challenging functionalization issues remains.[10] We introduce here the assembly of such hybrid materials from nano- and microcrystals of well-defined functionalized nanodiamonds (diamondoids) with transition metals. Diamondoids are sp^3-hybridized hydrocarbons that can be described as fully

hydrogen-terminated nanometer-sized diamonds.[11] They have been isolated in gram to ton quantities from petroleum,[12] allowing for their further C–H bond functionalization,[13] as the key step in the "bottom-up" processing of diamond-like structures. Nanodiamonds combine some unique features of both diamond and carbon nanostructures: they are structurally rigid,[14] thermodynamically stable,[15] exhibit large band gaps,[16] and size-tunable optical responses.[17] In the field of carbon nanomaterials, sp^3-carbon based diamondoid derivatives[18] complement sp^2-carbon based materials.[19] Few approaches have been described that relate to the goal of building ordered metal/sp^3-carboncage-based composites: (*1*) A way to form materials from diamondoids at the nanoscale has been to use their self-assembly properties on metal surfaces. Thus, thiol-functionalized diamondoids arrange into monolayers on gold and silver surfaces by dip-coating, affording hybrid layered materials with high yielding monochromatic photoemission.[18a, 18b, 20] (*2*) Phosphonic dichloride monolayers were prepared in solution by attachment to tungsten oxide via P–O bond formation. The covalent attachment improved the bond stability between diamondoids and the surface, and composites were found to be stable up to 350 °C.[21] (*3*) Self-assembly of plasma-hydrogenated detonation nanodiamond mixtures as aggregates in solution was described and heavily depends on the counter ions.[22] (*4*) Some diamondoid-based compounds combined with transition metals also exist as clusters or metal oxide-organic frameworks (MOFs).[23]

Still, the controlled nucleation and growth of metals, either as nanoparticles or thin films, specifically at the surface of perfectly-defined 3D sp^3-carbon cages is a hitherto unmet challenge we propose to solve with adequately functionalized diamondoid exploitation. Here we report a novel approach for the bottom-up construction of hybrid carbon nanostructures with an intimate arrangement between sp^3-carbon cages and a nanolayer of a transition metal. Such composites inverse the traditional building of MOFs and self-assemblies (metal first then organics), and as such it aims at delivering metal surfaces with modified properties from the sp^3-carbon core. Our

construction process is conducted stepwisely from the gas phase, using controlled vapor phase self-assembly of primary phosphine diamantane derivatives, followed by chemical vapor deposition of an organometallic complex under mild conditions over the self-assembled functionalized diamondoid scaffold. CVD is conducted at low temperatures, thus preserving the integrity of thermally sensitive materials.[24] We show that phosphorus functionalized diamantanes form well-defined self-assembled deposits on silicon substrates. The use of primary diamantane phosphine and phosphine oxide self-assembly yield new hybrid diamondoid-palladium core-shell organohybrid materials with thin palladium nanolayers as surface (below 10 nm) specifically covering the diamantane phosphine crystals. SEM and TEM microscopies combined with XPS and EDX analyses confirmed qualitatively and quantitatively the formation of a unique organohybrid, for which "Pd–O–PH–diamantane" interaction scheme is demonstrated by detailed XPS other all these elements. Such a bottom-up composite building process bridges scales from the molecular regime (functionalized diamondoids) to microscopic regime (metallic organohybrid) in the challenging association of a transition metal with an electronically saturated sp^3-carbon organic host material.

2. Results and Discussion

2.1. Self-assembly of functionalized diamondoids from the vapor phase

To complement the integration of diamondoids into composite materials from solution chemistry,[18a, 21, 23b] we reported convenient vapor deposition techniques of a wide range of functionalized diamondoids that provided robust nano- and microstructured self-assemblies of adamantane and diamantane derivatives bearing halogen or hydroxyl groups.[25] The absence of solvent in coating processes results in both better structuration and higher purity of the deposits. Based on the volatility of adamantane and diamantane derivatives,[26] physical vapor deposition

of functionalized nanodiamonds is a general and convenient method for accessing a variety of self-assembled uniform carbon nano- and microstructures (**Figure 1**).

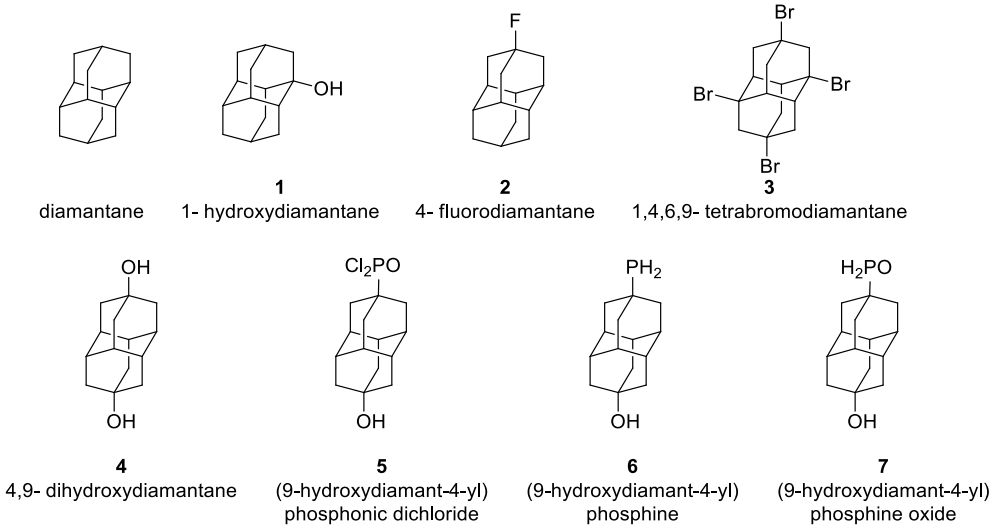

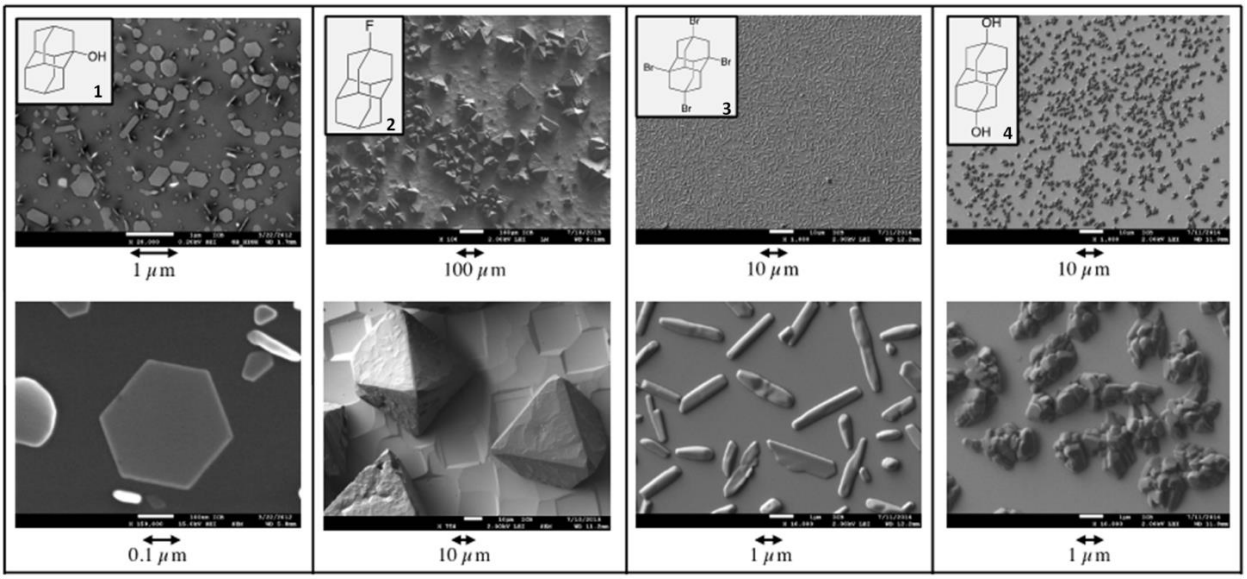

Figure 1. Top: Functionalized diamantane structures. Bottom: self-assembly of functionalized diamondoids from their vapor phase: 1-hydroxydiamantane (**1**),[25] 4-fluorodiamantane (**2**),[25] 1,4,6,9-tetrabromodiamantane (**3**), and 4,9-dihydroxydiamantane (**4**).

Such structures cannot be realized by classical dip coating, making controlled vapor deposition for diamondoid coatings a very promising method (details of vapor deposition process are given in *Supporting Information*, **Figure S1**). The resulting robust self-assemblies formed were used

herein as a convenient core-platform for further metal-carbon materials building. We introduced for the first time mild chemical vapor deposition (CVD) of organometallic precursors onto well-defined functionalized diamantane assemblies.

2.2. Pd deposition on hydroxy and fluoro functionalized diamantane self-assembly

We initially intended to control nucleation and growth of palladium nanostructures from decomposition of [Pd(η^3-allyl)Cp] on sp^3-C substrates starting from self-assembly of hydroxylated diamantane derivatives. This was investigated because the presence of hydroxyl groups on TiO_2 and SiO_2 substrates is known to be responsible for creating new nucleation sites for high rates of deposition of palladium particles with a narrow size distribution.[27] In the latter case, proton-induced decomposition of the palladium organometallic precursor [Pd(η^3-allyl)Cp] on the surface silanol OH groups accelerate an autocatalytic decomposition process. We first checked that [Pd(η^3-allyl)Cp] vaporization (sublimation enthalpy ΔH^0 = 81 kJmol^{-1})[24b] is fully compatible with the lower vapor pressure measured for functionalized diamondoids (ΔH^0 > 95 kJmol^{-1}).[25] The [Pd(η^3-allyl)Cp] complex decomposes at 260 ºC in the absence of a reactive gas such as O_2 or H_2 during the deposition process.[28] However, the temperature of decomposition can be lowered to 30 ºC at low H_2 partial pressure.[24b, 24c] Such mild CVD conditions yielded highly pure palladium deposits *via* a clean hydrogenation process. Accordingly, palladium deposition has been studied and various applications relating to palladium aggregates preparation are reported.[29] Herein, we achieved chemical vapor deposition of [Pd(η^3-allyl)Cp] (conditions in **Figure 2**) on pure crystals of 1-hydroxydiamantane (**1**). These were beforehand self-assembled onto silicon substrates by sublimation under low pressure (5 mbar, 80 °C). A similar process was used for the self-assembly of 4-fluorodiamantane (**2**) microcrystals. The resulting deposits were analyzed by SEM and *in situ* EDX analysis (**Figure 2** for **1**, and **Figure S2** for **2**). Contrary to our expectation, palladium

deposition did not occur on the microcrystal self-assemblies of **1** and **2**. Instead, cauliflower-like grain agglomeration, with a 100–160 nm size range, preferentially deposited onto the silicon substrate (SEM micrograph in **Figure 2**, zone 1). This deposition morphology is typical for the first stages of palladium thin film deposition on planar silicon-based substrates.[24c, 29e]

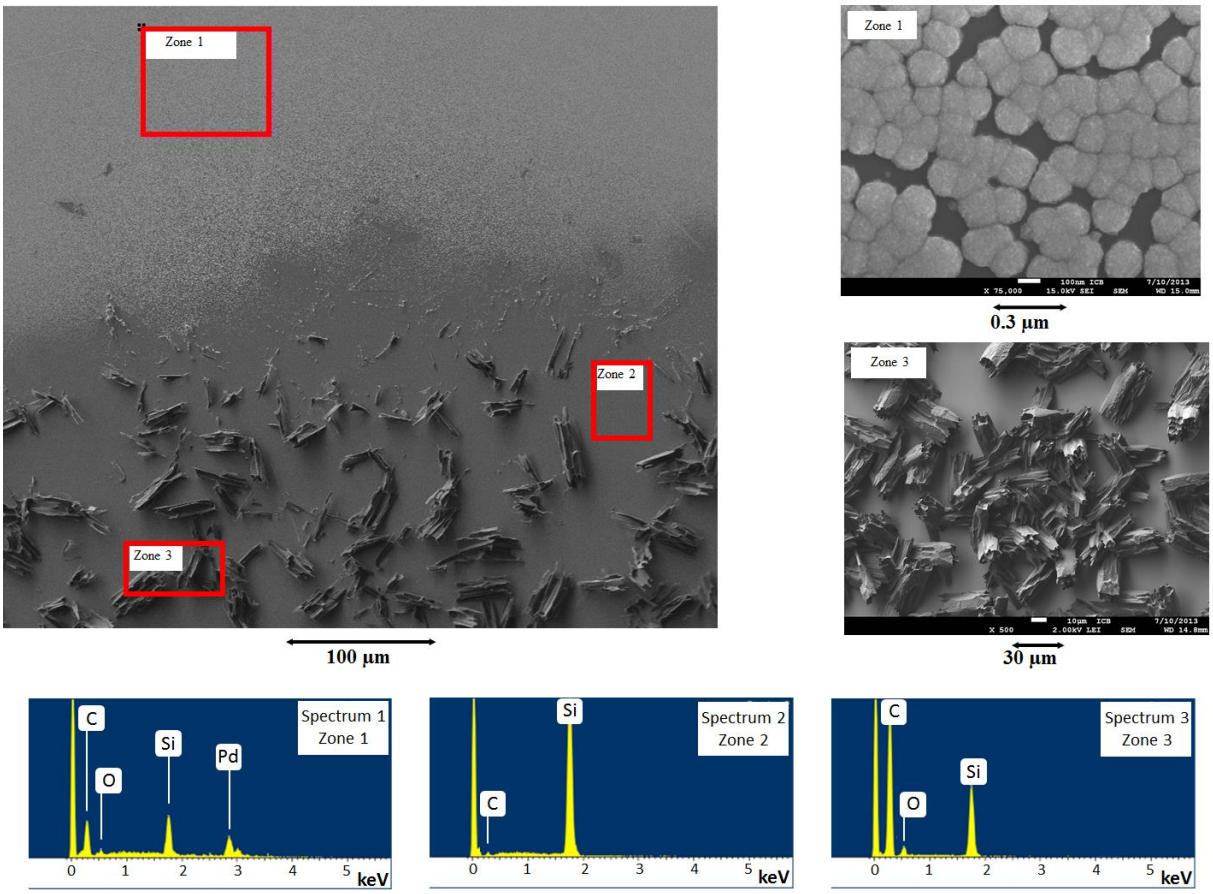

Figure 2. Palladium deposit on microcrystals of **1** (CVD conditions: 65 °C, 68 mbar, 30 min, 80 mL min^{-1} Ar flow and 2% vol. H_2 flow 1.6 mL min^{-1}) with enhancement and EDX spectra for zones 1 to 3.

EDX analysis focused at the Pd deposit achieved on nanodiamonds **1** shown in zone 3 of **Figure 2**, exclusively detected elements from the diamondoid substrate and the silicon support (C and O at 0.3 eV and 0.55 eV); palladium signals are absent (**Figure 2**, spectrum 3). Conversely, the presence of palladium in zone 1 was evident from the expected peak at 2.85 keV (**Figure 2**, spectrum 1). This implies a rather low affinity between **1** and Pd. The same phenomenon was

observed for fluorodiamantane (**2**) with a selective deposition of palladium onto the silicon substrate avoiding the sp^3-carbon cages (**Figure S2**). Clearly, the areas covered with nanodiamonds **1** and **2** disfavored metal palladium deposit nucleation. The high reactivity of palladium towards Si–OH bonds and clean Si–H surfaces has been reported,[24b] and the deposition mechanisms were studied for [Pd(η^3-allyl)Cp].[29e] On silicon-based substrates, hydrogen or hydroxyl-terminated surfaces exhibit high affinity for the deposition of [Pd(η^3-allyl)Cp] as a result of Si–H bond breaking. The hydroxy groups of Si–OH are considered as anchoring sites responsible for the dissociative adsorption of this precursor, while SiO_2 surfaces are unreactive.[30] After this first anchoring, the organometallic precursor decomposes readily on the surface leading to rapid autocatalytic Pd(0) deposition.[29c] Our present results show that in the competition for adsorption/decomposition of [Pd(η^3-allyl)Cp] over Si–H/Si–OH (*silicon surface*) or over C–H/C–OH and C–H/C–F sites (*diamondoid substrate*), the former is favored. There is no straightforward explanation for these experimental results since the binding energies fall in similar ranges (around 400 kJ mol^{-1}). However, the chemical stability of diamondoids is well-known,[11b] and might account for this bottleneck. To overcome this reactivity problem we focused at increasing palladium bonding affinity to the sp^3-cages via further functionalization.

2.3. Self-assembly of diamantane phosphine derivatives for metal deposition

Since the formation of metal nanocomposite materials from nanodiamonds **1** and **2** with palladium could not be conveniently achieved, we envisaged the introduction of phosphorus groups on diamantane with the idea in mind that these functional groups might strongly coordinate the top-layer palladium atoms, and in turn initiate nucleation and growth of metal organohybrid materials. The approach of controlled metal CVD onto functionalized sp^3-C based substrates has not been described. Notably, modifications of SiO_2 and Ta oxidized surfaces with an atomic layer of phosphorus deposited via a PH_3/He plasma at 255 °C have been reported,[31]

which led to palladium deposition from [Pd(hexafluoropentanedionate)$_2$] at 180 °C because of improved surface wetting and metal adhesion.

Recently, diamantane derivatives bearing both phosphonate and hydroxy groups have been synthesized by direct C−H bond functionalization preserving the –P(O)Cl$_2$ group in **5** (**Scheme 1**);[32] reduction of the phosphonate gives access to primary diamantyl phosphine **6**. Because of its remarkable air stability despite being a primary phosphine, we considered **6** as a pertinent candidate for vapor deposition to grow nanodiamonds-palladium organohybrid.

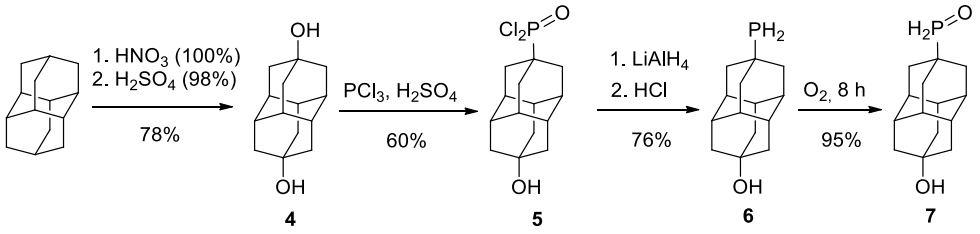

Scheme 1. Difunctionalized phosphorus-containing diamantanes **5**–**7**.

We first successfully achieved vapor phase self-assembly of microcrystals from phosphonate **5** on Si wafers (**Figure 3**). The self-assembly of **5** as microcrystals resulted in microstructures very different from those of the self-assemblies of fluoro- and hydroxydiamantane (**Figure 1**).

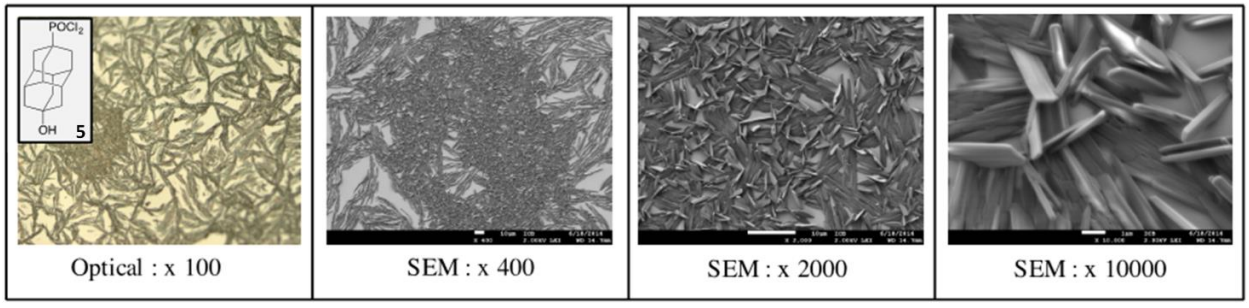

Figure 3. Optical and SEM images of phosphoryl diamantane **5** self-assembled by vapor deposition (85 °C, sublimation under 4 mbar dynamic vacuum, 2 min).

The optical microscopy images indicate a homogeneous distribution of crystals in a pine leave-like arrangement on the Si wafer. The SEM images show that diamondoid particles mostly grew as regular platelets with a remarkable morphological unity of shape and size (about 2.4 µm x 0.5 µm and a thickness of around 0.24 µm). These platelets cover large areas without preferential orientation and were found to be resistant to vacuum and the beam energies used in the SEM analyses. Then, self-assembly of **6** on Si wafer was also achieved under dynamic vacuum at 85 °C. Optical microscopy images revealed well-dispersed rod-like materials (**Figure 4**).

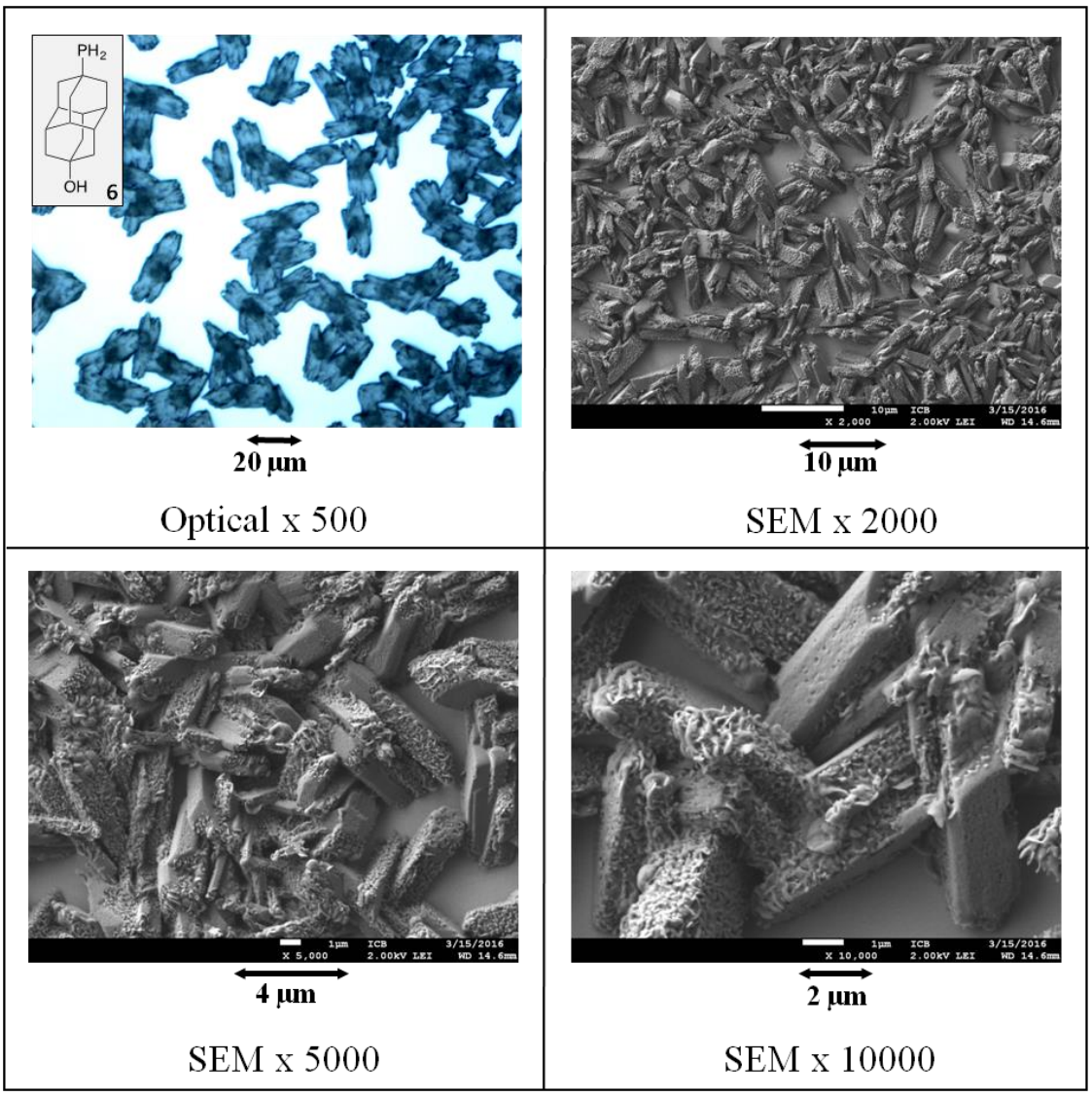

Figure 4. Optical and SEM images of phosphine diamantane **6** self-assembly by vapor deposition under high vapor supersaturation. PVD conditions: 20 °C →85 °C in 2 min, then 2 min at 85 °C, 4 mbar dynamic vacuum.

SEM images of the self-assembly show the formation of interpenetrating compact polyhedral microcrystals of about 1.0 to 2.5 μm. Additionally, SEM enhancements (**Figure 4**, x5000 and x10000) show a particularly rough surface of the rods that was not observed for the previous microcrystals self-assembly of **1**–**5**. A high supersaturation ratio from the vapor phase greatly favors nucleation (**Figure 4**) in comparison with the growth rate (**Figure 5**),[24c] and results in the nucleation of a large number of small crystallites.

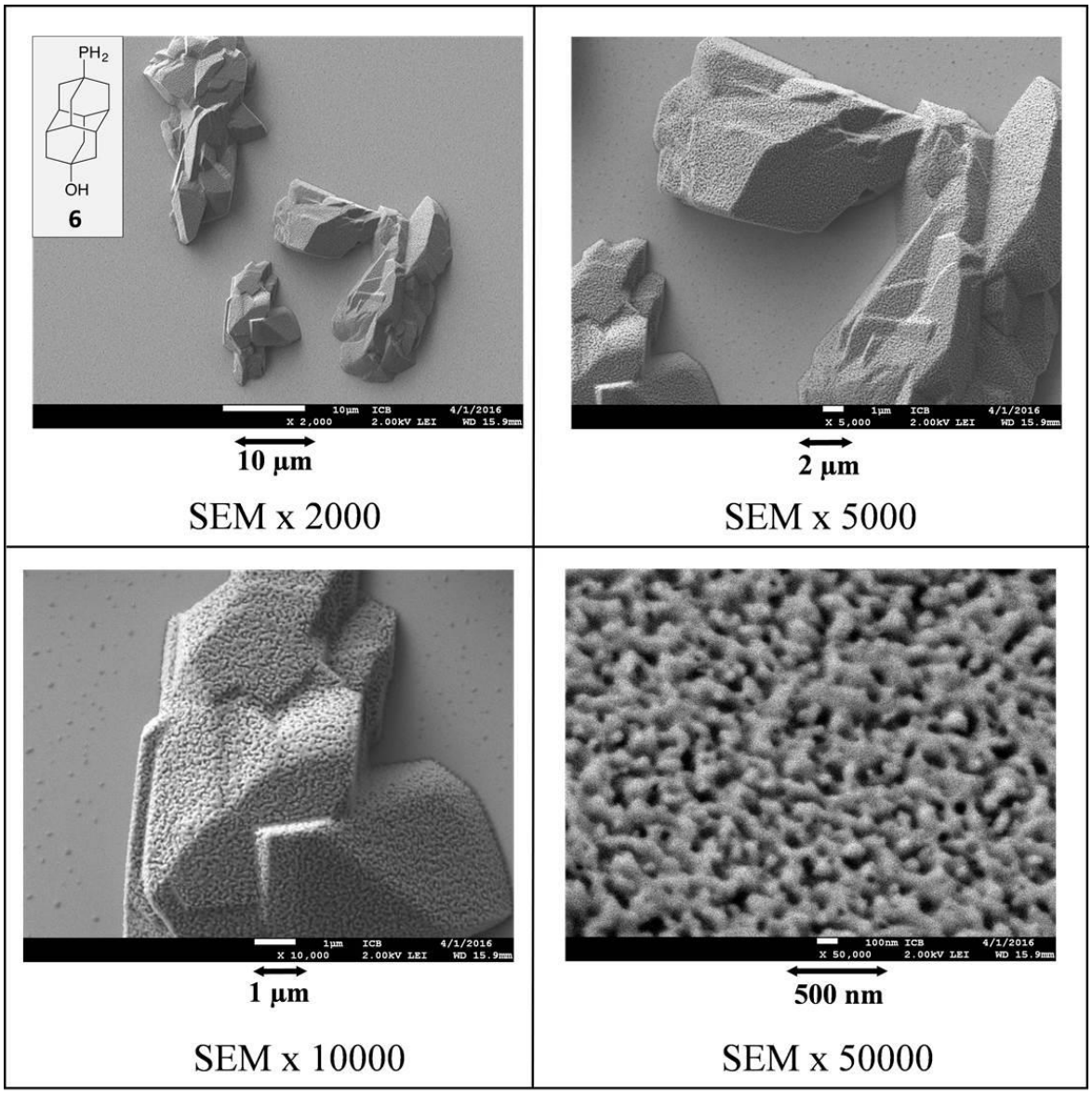

Figure 5. SEM images of phosphine diamantane **6** self-assembly by vapor deposition under lower supersaturation regime. PVD conditions: 20 °C→65 °C in 15 min, then 105 min at 65 °C, 5 mbar dynamic vacuum.

The initial conditions used for sublimation of **6** favored a high supersaturation ratio of diamondoids in the gas phase because of the fairly high temperature of 85 °C. To confirm the propensity of **6** to produce microcrystals with rough surfaces independently of the vapor pressure regime, we tuned the conditions to favor slow growth of bigger crystals at lower supersaturation ratios. Self-assembly from vapor deposition of **6** under dynamic vacuum at 65 °C applying a low temperature slope and 5 mbar for 120 min (**Figure 5**) successfully resulted in a controlled growth of fewer but bigger, still polyhedral microcrystals. These consist of truncated polyhedrons with a length size of about 10 to 30 μm. The high surface roughness remains still characteristic for the vapor phase self-assembly of diamondoids **6**. The enhancement of micrographs (**Figure S3$_A$** and **Figure S3$_B$**) evidenced the distribution of regular cavities at the surface centered around 50–100 nm. Self-assemblies by vapor deposition under vacuum for **5** and **6** were conducted several times and were fully reproducible. The self-assembled microcrystals of **5** and **6** were unchanged over the course of at least one week under ambient conditions in air without visible alteration of the structures and composition according to SEM and EDX analysis. With these preliminary results in hands we envisioned palladium deposition over P-functionalized nanodiamonds.

2.4 Palladium deposition on diamantane phosphonate dichloride 5

Palladium deposition was first attempted on the self-assembled microcrystals of **5** using [Pd(η^3-allyl)Cp] in the presence of 4 vol.% H_2. While we were not expecting the direct bonding of palladium to phosphorylated diamantane **5**, we hypothesized that the H_2 reductive atmosphere in the presence of palladium may help reduce –P(O)Cl_2 into –PCl_2, and thereby liberate specific anchoring sites for palladium to the diamondoid crystals via the available phosphorus lone-pair. This clearly failed and the short-time palladium deposition runs we conducted on **5** self-assembly were unsuccessful (45 °C, 50 min, **Figures S4–S6**). Forcing the conditions with 6 h

deposition time resulted in palladium nodules coverage all over the sample, both on platelets self-assembly of **5** and on the Si wafer where diamondoid self-assembly was absent (**Figure 6**, left).

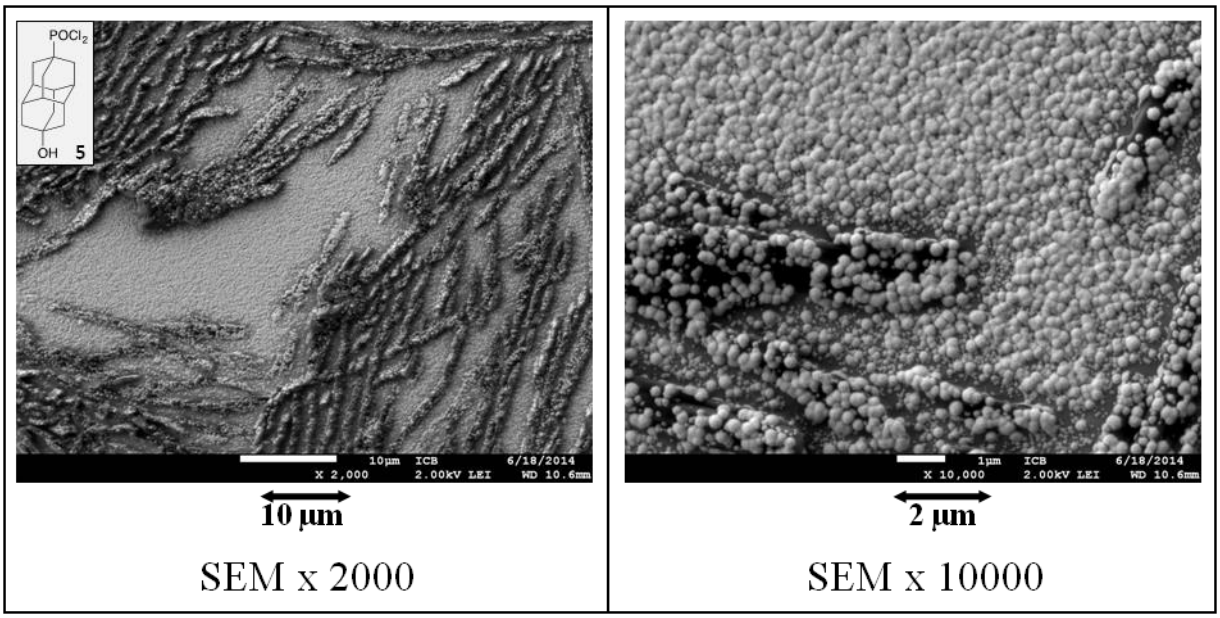

Figure 6. Palladium CVD on self-assembly of **5** (CVD conditions: 30 °C, 68 mbar, 360 min, 80 mL min^{-1}Ar flow, H_2 flow 3.2 mL min^{-1} 4% vol.).

Enhancement of the SEM images showed that palladium is deposited as spherical cauliflower-like particles with size ranging between 30 and 300 nm (**Figure 6**, right). This deposition mode is typical for decomposition of [Pd(η^3-allyl)Cp] on various inorganic substrates.[24b, 29e, 33] As such it does not indicate significant influence of the functionalized diamondoid towards the formation of nanocomposites. XPS surface analysis confirmed this assumption with classical Pd_{3d} signals obtained for metallic palladium aggregates. Again, the formation of organohybrid nanodiamonds-palladium failed evidencing a very challenging issue in the intimate construction of sp^3–C/metal scaffolds.

2.5 Palladium deposition on the primary diamantyl phosphine 6

We conducted palladium deposition using **6** as framework under similar conditions which combined reducing H_2 atmosphere with [Pd(η^3-allyl)Cp]. The resulting deposits successfully gave new nanodiamonds-palladium material **8** that was analyzed by SEM (**Figure 7**). Substantial changes were observed in comparison to the SEM of non-metalized self-assembly of **6** and palladium-CVD deposits that we previously achieved over nanodiamonds **1**, **2** and **5** (**Figure 2** and **Figure 6**).

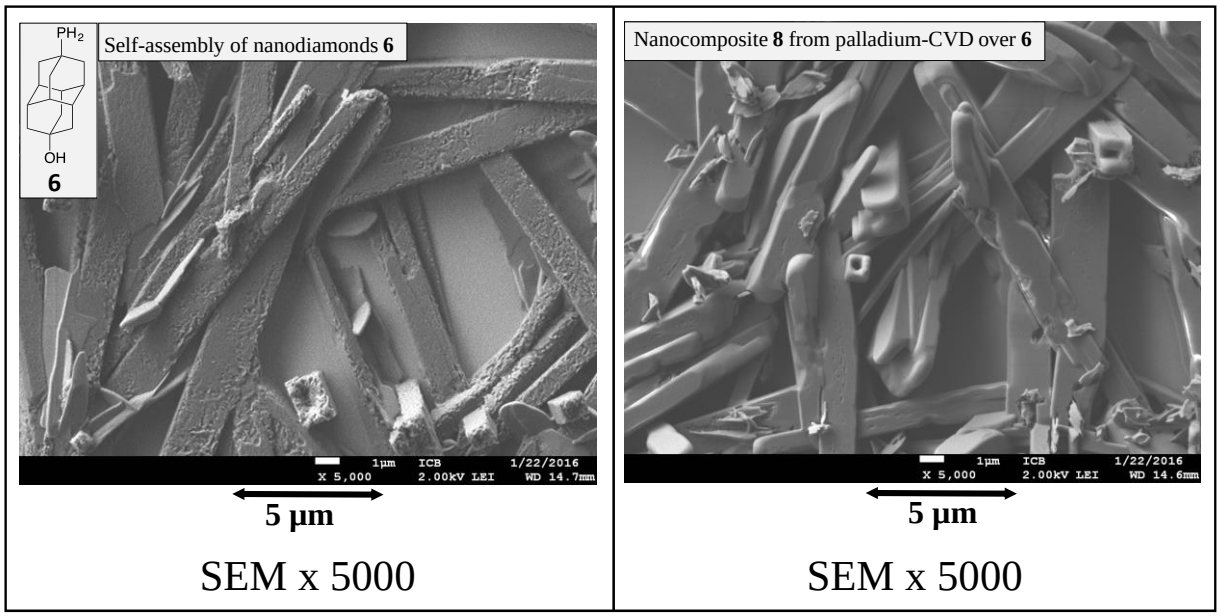

Figure 7. SEM images comparing surfaces of microcrystals self-assembly of **6** before (left) and after (right) low-temperature palladium CVD (CVD conditions: 45 °C, 67 mbar, 50 min, H_2 3.2 mL min^{-1}).

In the SEM images, smoothing of the nanodiamonds microcrystal surface is visible after palladium-CVD (details in **Figure S7**), while their bulk morphology was not altered. The palladium nodules which were previously observed from [Pd(η^3-allyl)Cp] deposition under H_2 atmosphere using the other nanodiamonds clearly did not form in this case. The fading of surface roughness of **6** was consistently observed and correlated with the ICP-MS (Inductive Coupled

Plasma Mass Spectrometry) analysis of the samples, which indicated the presence of palladium element in 0.3 to 0.4% wt. No bulk palladium formation as a thick film or aggregates could be detected in the entire deposit we examined by combination of SEM, TEM and EDX. Clearly, while TEM cartography identified all the elements (C, O, P, Pd, **Figure S8**), EDX analysis of these samples conducted over various regions failed to detect typical signals associated with palladium aggregates (**Figure 2**, spectrum 1, 3.0 keV) correlating that the presence of palladium detected by ICP-MS is explained only by a thin surface layer over the diamondoid scaffolds.

2.6. Structural analysis of nanodiamonds-palladium core-shell organohybrid 8

The unexpected diamondoid surface smoothing observed after palladium deposition experiments may result from either a large scale surface rearrangement of the self-assembly of **6** or may be due to, as postulated, the growth of a palladium metal layer on top of the organic substrate, thereby filling the surface cavity of the self-assembly of **6**. To characterize the surface modifications, we operated blank CVD experiments (details in **Figure S7**). The SEM analysis confirmed that smoothing of the surface occurred only upon deposition of palladium using H_2, and that it is clearly not due to thermal rearrangement. XPS surface analysis of the self-assembly of **6** on a silicon wafer before Pd-deposition identifies all expected elements according to their core levels (**Figure 8**): C (C_{1s} 283.5 eV), P (P_{2p} 132.1 eV), O (O_{1s} 531.2 eV), and Si (from the silicon wafer).

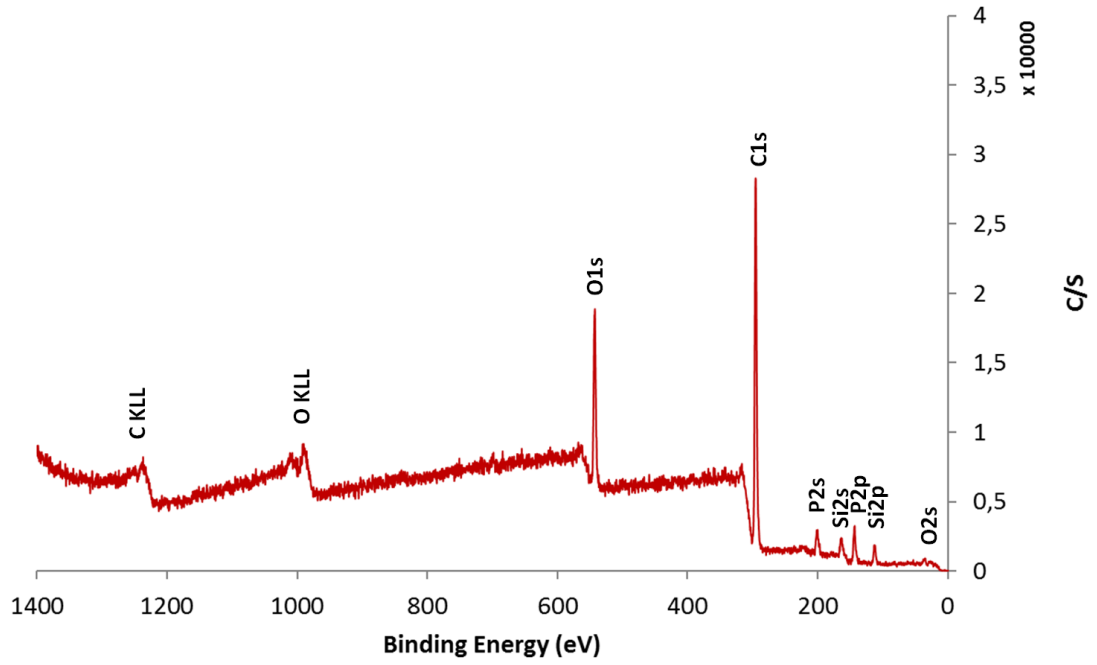

Figure 8. XPS of microcrystals self-assembly of **6** on a silicon wafer (before Pd-CVD).

The atomic content ratio of elements was determined as carbon 68.7%, oxygen 11.5%, and phosphorus 4.8%. This ratio is expected to be close to 14/1/1 for pure diamantyl phosphine **6** ($C_{14}H_{21}OP$). The C/P ratio was found to be 14.3 (**Table 1**), consistent with the theoretical value for **6**, showing that surface carbon contamination of the samples is very limited. The P/O ratio is equal to 2.4 evidencing conversely that phosphine oxide **7** is largely present on the surface layers for the analyzed depth of less than 10 nm.

The XPS analysis of nanodiamonds-palladium composite **8** (**Figure 9**), which was obtained after palladium CVD over the self-assembled microcrystals of **6** identified all the expected elements on the surface: C (C_{1s}, 283.6 eV), P (P_{2p}, 132.1 eV), O (O_{1s}, 531.2 eV), and especially palladium with binding energy values (BE) $Pd_{3d3/2}$ at 336.3 eV and $Pd_{3d5/2}$ at 341.6 eV, and Si from the wafer support.

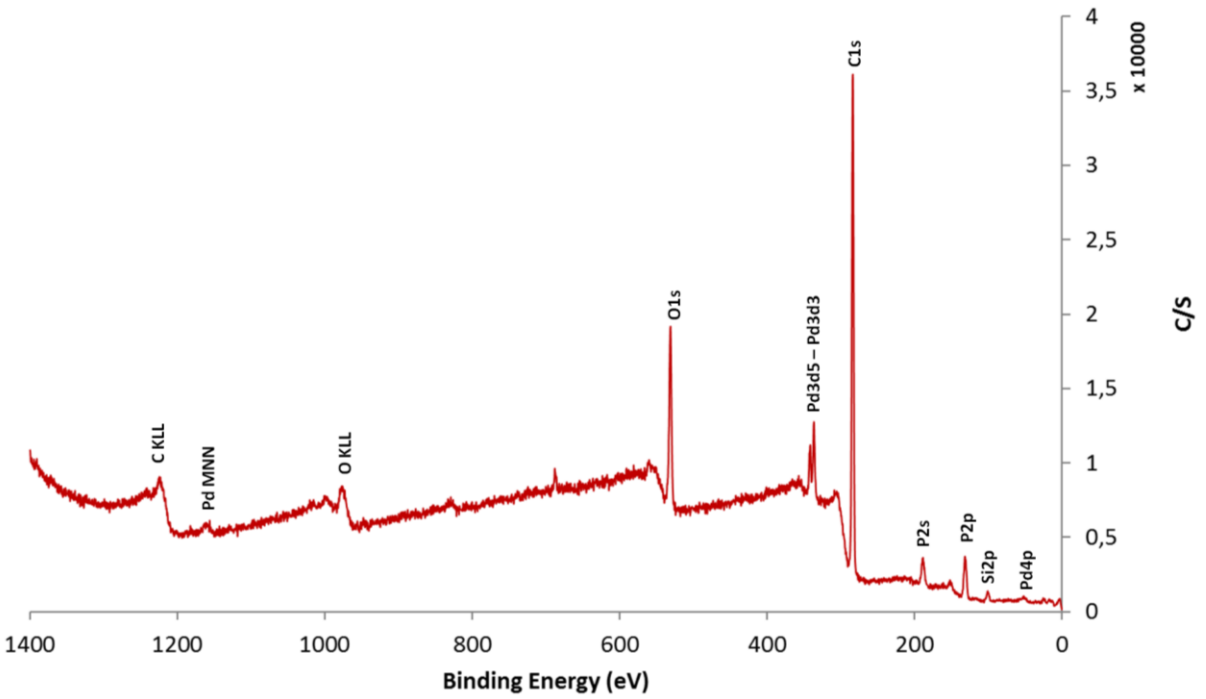

Figure 9. Survey XPS spectrum of nanodiamonds-palladium composite **8**.

From the XPS surface analysis of **8** we determined the atomic content for carbon 74.8%, for palladium 0.8%, and for phosphorus 5.2%; indicating a Pd/P ratio of 0.15, and a C/P ratio of 14.4. The low palladium content correlates with the absence of bulk palladium nodules. Therefore, consistent with the EDX analysis that was found silent for palladium detection, palladium is mainly present at the surface of the diamondoid self-assembly in the form of very thin layers (*Note*: EDX bulk analysis has a depth of about 1 μm, against less than 10 nm for XPS surface analysis). **Table 1** gathers data concerning the atomic content ratios for **6** and **8** normalized to one phosphorus atom. The analysis of oxygen region for diamondoid **6** and hybrid **8** is also informative. Notably, the KLL O/C ratio value for Auger electrons[34] (**Table 1**, entry 1) is found to be much higher before Pd-CVD (1.22 *vs* 0.61) than after Pd-CVD. This indicates that phosphine oxide **7** (**Scheme 1**) that forms on the surface of self-assembled **6** in significant quantity (see above) partially undergoes reduction in the Pd-deposition process and the oxygen/carbon ratio diminishes. The O_{1s}/P_{2p} ratio confirmed this observation, showing lower

oxygen content in **8** (thus after palladium deposition, **Table 1**, entry 2). The reductive conditions of deposits with H_2 and the effective palladium deposition are consistent with these results.

Table 1: Atomic ratio for self-assembly of diamondoids **6** and for nanocomposite **8**.

Entry		Before Pd-CVD (**6**)	After Pd-CVD (**8**)
1	$KLL_{O/C}$	1.22	0.61
2	O_{1s}	2.4	2
3	C_{1s}	14.3	14.4
4	P_{2p}	1	1
5	Pd_{3d}	/	0.15

*2.6.1. Detailed XPS surface analysis of nanocomposite **8** in the palladium Pd3d region.*

The nanodiamonds-palladium hybrid **8** formed with a core of sp^3-C from diamantane and a thin layer of palladium was examined further. We used a *standard metallic palladium sample* (labeled **9**), which consisted of bulk palladium aggregates (or nodules) supported on a Si wafer, as it is typically obtained from palladium CVD on inorganic supports (**Table 2** for literature data, **Figure 10** for our experimental data). The $Pd3d_{5/2}$ binding energies for metallic Pd(0) (**Table 2**, entries 1 and 4) are expected between 334.6–335.4 eV with a characteristic dissymmetric shape (Doniac-Sunjic profile) for the doublet.[35] The standard sample **9** (**Figure 10**, top) perfectly fits these features with peaks found for $Pd3d_{5/2}$ at 335.0 eV and $Pd3d_{3/2}$ 340.7 eV (**Table 2**, entry 5).

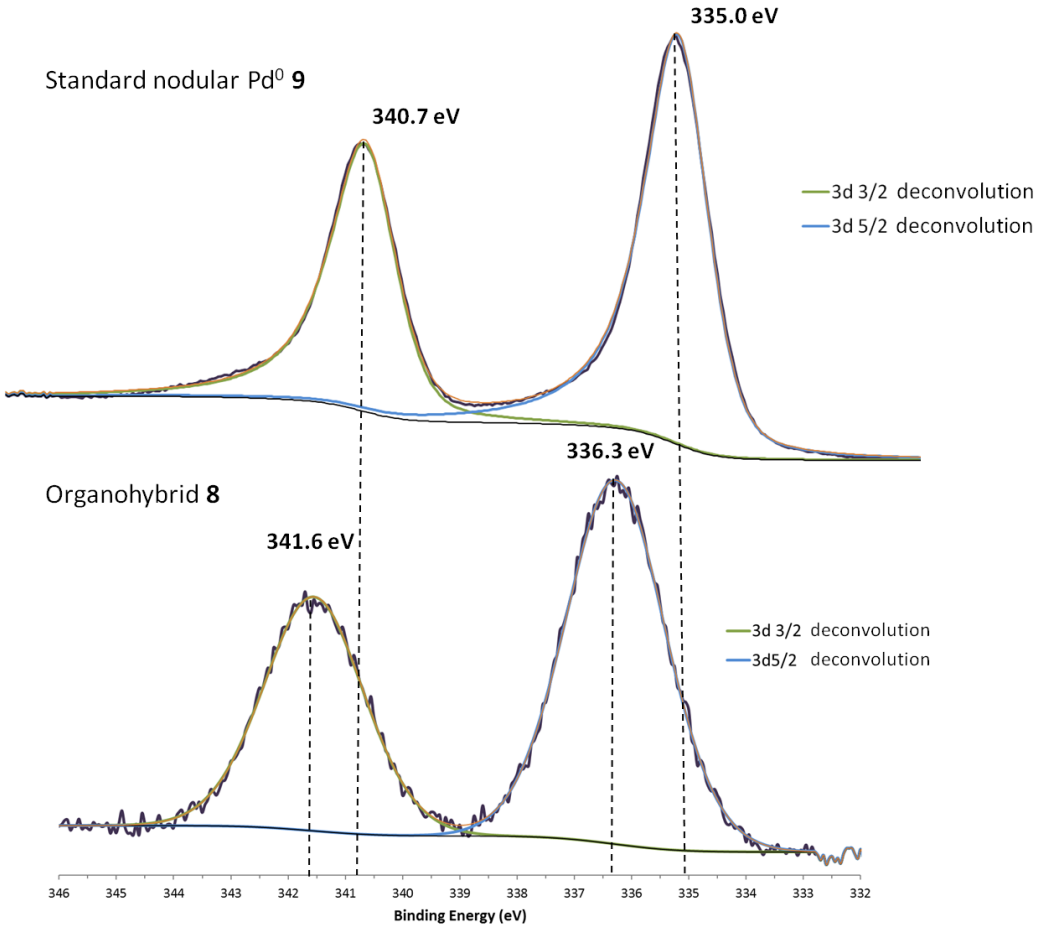

Figure 10. Comparative high-resolution XPS spectra at Pd3d binding energy of standard deposition of nodular metallic Pd(0) over Si wafer **9** and organohybrid **8**. Blue and green lines are deconvolution for $3d_{5/2}$ and $3d_{3/2}$, respectively.

XPS surface analysis of **9** shows high purity and does not exhibit any PdO_x signal. For the nanocomposite **8** the Pd binding energies are shifted towards higher energy (Δ =1.3 eV) with now clearly symmetrical peaks found for $Pd3d_{5/2}$ at 336.3 eV and for $Pd3d_{3/2}$ at 341.6 eV (**Table 2**, entry 6). Deconvolution of the Pd_{3d} signals for **8** adequately fits a unique doublet (**Figure 10**, bottom), indicating without ambiguity that palladium is present in a single well-defined phase having similar environment for palladium atoms.

Table 2: Literature XPS binding energy for $Pd^{(II)}$ and $Pd^{(0)}$ materials and complexes.

entry	Surface material–Support	XPS $Pd_{3d5/2}$ BE (eV)	Ref.
1	Pd–inorganic metal or oxide	334.6–335.4	[35]
2	PdO–inorganic metal or oxide	336.6–336.9	[35],[36]
3	PdO_2–inorganic phase	337.7	[37]
4	Pd–Pd(111)	335.1	[29b]
5	Pd–Si wafer standard **9**	**335.0**	this work
6	Nanocomposite **8**	**336.3**	this work
7	Pd–$[P_x]SiO_2$	335.8	[31]
8	$Pd(PPh_3)_4$/ n. s.	336.2	[38]
9	$[Pd_2(PPh_3)_2]$ / n. s.	336.4	[37]
10	Pd(η^3-allyl)Cp–Pd(111)	337.7	[29b]
11	$[Pd(OAc)_2]_n$/ n. s.	338.8	[38]

n. s. = no support.

The XPS values found for **8** at $Pd3d_{5/2}$ 336.3 eV (and $Pd3d_{3/2}$ at 341.6 eV) approach literature assignments for Pd–O bonding, ranging *ca.* 336.6–336.9 eV for $Pd3d_{5/2}$ (**Table 2**, entry 2). These values are also fairly close to the energy values reported for Pd–P bonding in non-supported complexes (which is clearly not the case of **8**) such as $[Pd^{(0)}(PPh_3)_4]$ ($Pd3d_{5/2}$336.2 eV, **Table 2**, entry 8) and $[Pd_2^{(0)}(PPh_3)_2]$ ($Pd3d_{5/2}$336.4 eV, **Table 2**, entry 9). Palladium nanocomposite **8** accounts for binding energy values that are also higher than palladium deposited on SiO_2 surfaces modified by high temperature implantation of an atomic layer of phosphorus Pd@$[P_x]SiO_2$,[31] for which $Pd3d_{5/2}$ BE has been found at 335.8 eV (**Table 2**, entry 7). Nevertheless, the Pd3d binding energy values for **8** were clearly not attributable to adsorbed molecular Pd^{2+} complexes for which BE values are higher than 337 eV. For instance the values of $[Pd^{(II)}(\eta^3$-allyl)Cp] deposited on Pd(111) single crystal are reported as $Pd3d_{5/2}$BE 337.7 eV

(**Table 2**, entry 10),[29b] and [$Pd^{(II)}(OAc)_2$] BE 338.6 eV (**Table 2**, entry 11).[38] Fine understanding of palladium bonding scheme in nanocomposite **8** needs the detailed surface analysis of P and O regions in XPS.

*2.6.2. Detailed XPS surface analysis of nanocomposite **8** in the phosphorus P2p region.*

XPS analysis in the phosphorus region was achieved by comparing the microcrystal self-assembly of **6** with those of nanocomposite **8** formed after Pd-CVD (**Figure 11**). The BE value associated to **6** is found at 129.2 eV (the P2p BE value for free triaryl phosphine PPh_3 has been reported to be 130.9 eV).[38] The other dominant component (*ca.* 90%) at higher BE 132.1 eV is attributed to phosphine oxide derivative **7** *mainly present on the surface* (caution: this is not the case in the bulk self-assembly, see morphology difference in the SI, **Fig. S10**). According to the literature, alkyl phosphine oxides have BE values of this order of magnitude (*e.g.*, 132.5 eV for trioctylphosphine oxide).[39] We have independently synthesized **7** (**Scheme 1**) and deposited it on a silicon wafer by PVD (**Figure S9**). The XPS spectra of P2p confirmed the binding energy peak at 132.1 eV for **7** (**Figure S10**).

XPS surface analysis of nanocomposite **8** in the BE area of phosphorus evidenced the influence of palladium deposition with a significant change in the appearance of the P2p line (**Figure 11**, bottom). Deconvolution attempts of this line in two components were inconsistent. However, three components deconvolution allowed distinguishing two rising peaks at 129.2 and 130.5 eV BE, which are consistently attributable to **6** and to the nanodiamonds-palladium hybrid **8**, respectively. The P2p peak at 132.1 eV attributed to phosphine oxide **7** is still dominant. The comparative rising of the signal of **6** is attributable to the diminishing of surface diamantyl phosphine oxide **7** turned into hybrid **8** by its binding to Pd. This is consistent with a linkage of Pd to the oxygen of **7** shifting in turn the BE for $P2_P$ from 132.1 eV to 130.5 eV (*i. e. a decrease of electron-withdrawing influence of oxygen over phosphorus from bonding with palladium*).

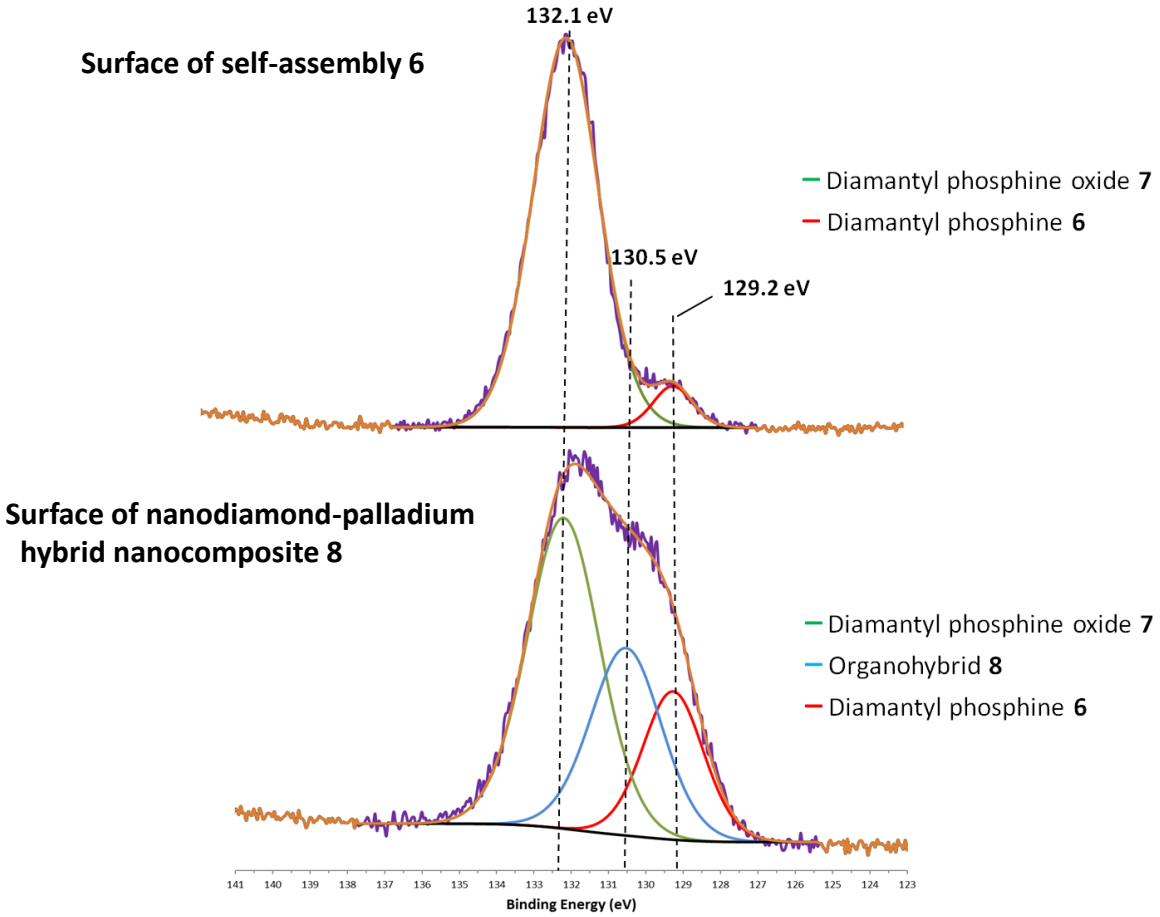

Figure 11. High-resolution XPS spectra at P2p binding energy for surface of self-assembly microcrystals **6** (top) and nanodiamonds-palladium organohybrid **8** (bottom). Green, blue, red lines are P2p deconvolution accounting for oxide **7**, hybrid **8**, and phosphine **6**, respectively.

Quantitative deconvolution of P2p line shows that *ca*. 30% of the surface phosphorus atoms belong to **8**. These P atoms are present *on the surface* and belong to the hybrid material (not to phosphorus from free oxide O=PH_2– and primary phosphine –PH_2). The BE of P2p peak corresponding to **8** (130.5 eV) is shifted to higher energy compared to pure **6** (129.2 eV), which indicates that the phosphorus atom cannot be directly bonded to palladium, but is more likely in a Pd–O–PH–R coordination scheme as depicted in **Figure 12**. The XPS analysis in O region (see below) confirmed this proposal.

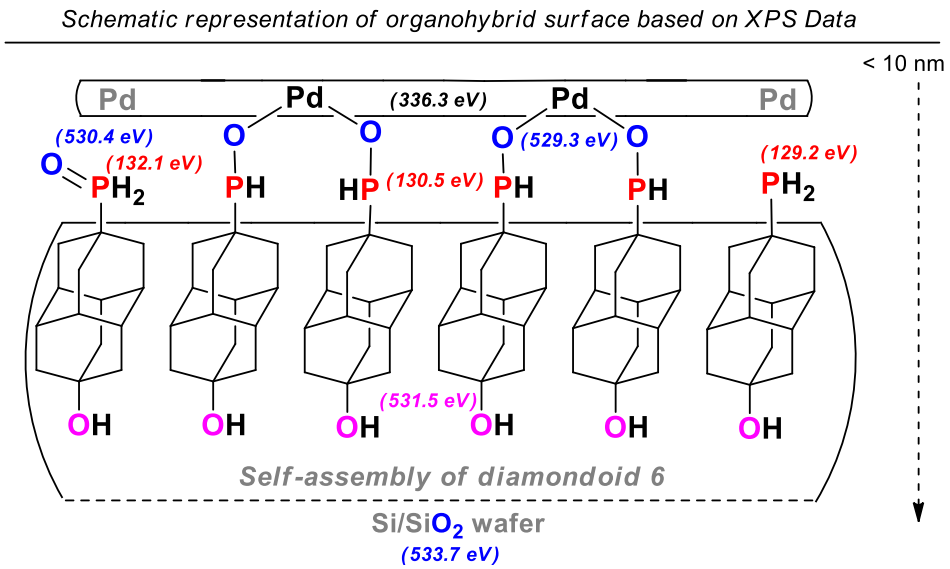

All BE of XPS are consistent with an electron transfer from the palladium metal layer to the sp^3-C organic core of the diamondoid self-assembly via O–P motif

Figure 12. Schematic model of nanocomposite **8** with a surface representation based on XPS data (*not excluding additional linkage possibilities Pd–Pd*). A stoichiometry of two molecules per Pd is quite consistent with the Pd/O/P atomic ratio and the deconvolution spectra (Pd: 0.15, P: 0.3, and O:0.2).

*2.6.3. Detailed XPS surface analysis of nanocomposite **8** in the oxygen O1s region*

To definitively assess Pd–O bonding in organohybrid **8** we analyzed XPS in the oxygen O1s region (**Figure 13**). Surface XPS of self-assembly of **6** (**Figure 13**, top) showed a signal that is appropriately deconvoluted in two BE peaks at 530.4 eV (*O*=P from **7**, *ca.* 45%) and 531.5 eV (C–*O*H from **6** and **7**, ca. 55%). The first peak at 530.4 eV is attributed to the P=O oxygen of **7** in accordance with XPS analysis at P2p region which showed that **6** is highly oxidized on the surface (about 90%).

XPS surface analysis of nanocomposite **8** in the BE area of oxygen showed that the deconvolution requires four components (**Figure 13**, bottom). The components at 531.5 eV (C–*O*H) and 530.4 eV (*O*=P) are still present. Two additional peaks were also visible at BE 533.7 eV (SiO_2 from wafer, *ca.* 12%) and at 529.3 eV (*ca.* 10%) the most shifted oxygen signal is

attributed to the oxygen linking palladium and phosphorus R–P–*O*–Pd. XPS at oxygen region is therefore fully consistent with both the palladium and the phosphorus XPS surface analysis.

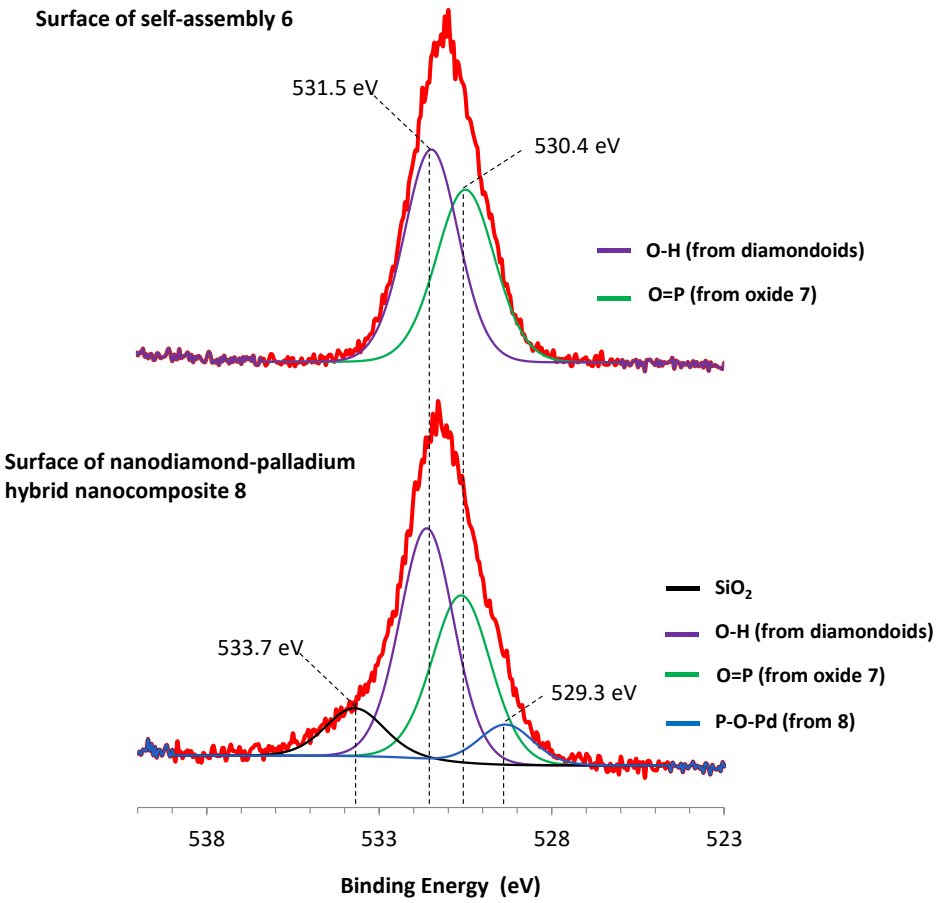

Figure 13. High-resolution XPS spectra comparison at O1s binding energy for surface of **6** self-assembly microcrystals (top) and nanodiamonds-palladium organohybrid **8** (bottom). Black, purple, green, blue, lines are O1s deconvolution.

When comparing the XPS data of **8** with XPS surface analysis of samples **6** and **9**, the BE shifts at higher energy in Pd3d region (**Figure 10**) and global BE shifts at lower energy in P2p (**Figure 11**) and O1s (**Figure 13**) region are consistent with an electron transfer from the palladium metal layer to the sp^3-C organic core of the diamondoid self-assembly via O–P motif. Reports about electron-deficient palladium ascribed to very small supported clusters evidenced by XPS spectroscopic shift showed that these materials affect the heterogeneous catalysis using

H_2 and olefins.[40] As such, electron-deficient nanolayered palladium surfaces may also find use in gas sensors field,[41] which may orientate relevant applications of these nanodiamonds-metal composites formed using this innovative successive vapor phases procedure.

Finally, we successfully extended this mild vapor-phase procedure enabling nanolayering metal onto functionalized sp^3-carbon to related nanodiamonds-platinum organohybrid formation. XPS survey of the nanodiamonds-platinum composite obtained from **6** (**Figure S12a-c**) fully confirmed the surface analysis achieved for **8** with analogous BE shifts obtained at Pt4f and P2p.

3. Conclusions

Functionalization of diamondoids with purpose-tailored groups –herein the primary phosphine and its oxide– give access to the unprecedented growth of palladium as a thin nanolayer on the surface of 3D sp^3-C-based organohybrid materials. Using molecular nanodiamonds turned out to be considerably more challenging than the synthesis of nanocomposites from sp^2-carbon materials that benefit from large aromatic domains or varied surface functional groups. Organic-inorganic diamondoid-palladium nanocomposites did not form from hydroxylated, fluorinated or phosphorylated diamantanes. Conversely, we use the primary diamantane phosphine **6** (4-hydroxy-9-phosphinodiamantane) after its vapor-phase self-assembly to build an unprecedented hybrid nanodiamonds-palladium core-shell structure. TEM and EDX analyses of the nanocomposites evidenced that no bulk palladium is present as aggregates or nodules, or thick films. SEM, ICP and detailed XPS analyses indicate that the 0.3–0.4 wt.% of detected palladium is located at the very surface of sp^3–C diamantane cages. High resolution XPS shows that the new hybrid nanodiamonds-palladium materials incorporate Pd–O–PH–diamantane bonding motifs. This vapor-phase method was successfully extended to platinum organohybrid formation. Thus, our approach opens a way to grow metal and metal oxide nanolayers on molecularly-defined nanodiamonds via P–H functionalized surfaces. The entirely vapor phase-

controlled mild synthetic process allows a new level of control over nanocomposite formation utilizing morphology from molecular-level modifications. As such, this bottom-up composite building process bridges scales from the molecular regime (functionalized diamondoids) over nanoscopic (self-assemblies) to microscopic regime (hybrid), in the challenging association of transition metals with an electronically saturated sp^3-C organic host materials.

4. Experimental Section

4.1. General Information. The synthesis of functionalized diamantanes was achieved using Schlenk techniques. Glassware was dried in an oven at 110 °C before use. Tetrahydrofuran (THF) was dried on activated molecular sieves 4 Å. $CDCl_3$ was dried over activated 4 Å molecular sieves under argon. The other solvents were obtained directly from the manufacturer or distilled from technical grade. Commercially available reagents were used without further purification. TLC was done on 0.2 mm silica gel with fluorescent indicator (pre-coated polyester sheets UV_{254} or TLC silica gel 60 F_{254} on aluminum sheets). Column chromatography was done on silica gel (70–230/100–160/230–400 mesh ASTM). NMR spectra were recorded at 300, 400, 500, and 600 MHz spectrometers with TMS as internal standard.

XPS spectra were recorded with a PHI Versaprobe 5000 apparatus using monochromatic Al Kα X-ray (1486.6 eV). The average circular spot size is 200 μm diameter. High-resolution scans were acquired using a Pass energy of 20 eV and 45° emission angle. These measurements were carried out at room temperature inside a vacuum compartment under pressure of 10^{-6} Pa. As the samples are insulators, a low-energy (<10 eV) electron flood was used to neutralize the surface charge caused by photoelectron emission. The XPS data were then calibrated according to the sp^3 component of C1s line (283.5 eV). A standard CASA-XPS software package was used for data analysis, especially the deconvolution of lines and calculation of atomic ratios using R.S.F. given by the software.

SEM images were recorded with JEOL JSM 7600F and EDX spectra were recorded using SDD Oxford (80 mm^2, 129 eV KαMn).

4.2. Diamantane derivative syntheses. These syntheses were done as previously described.[32] Spectral data are available in the SI and are identical to those reported.

(9-hydroxydiamant-4-yl)phosphine oxide (7): The oxide was synthesized from a solution of **6** in CH_2Cl_2 using compressed air bubbling for 8 h (yield 95%, purity 95%+, traces of **6**). ^1H NMR

(500 MHz, 298 K, $CDCl_3$): δ=6.65 (d, 1H, $J_{P–H}$ = 450 Hz), 1.98 (br s, 6H), 2.10 (br s, 3H), 1.97 (br s, 2H), 1.93 (br s, 3H), 1.86 (m, 4H), 1.75 (m, 7H), 1.25 (br s, 1H, OH) ppm. ^{13}C NMR (125 MHz, 298 K, $CDCl_3$): δ=67.0 (s, C_q), 44.9 (d, *J* = 190 Hz, CH_2), 38.9 (d, *J* = 5 Hz, CH), 37.3 (s, C_q), 35.2 (d, *J* = 50 Hz, CH), 34.5 (s, CH_2) ppm. $^{31}P\{^1H\}$ NMR (202 MHz, 298 K, $CDCl_3$) δ=27.84 ppm. HRMS (EI): *m/z* $[M+H]^+$ calcd for $C_{14}H_{21}O_2P$: 253.1352; found: 253.1356, [err] 2.38 ppm.

Supporting Information

Additional data include ^1H, ^{13}C, ^{31}P NMR spectra for diamondoids **5**–**7**and ^1H for [Pd(η^3-allyl)Cp)], SEM and EDX data for **2** self-assembly and ensuing Pd-CVD, microscopy and XPS analysis for phosphonic dichloride **5** self-assembly and ensuing Pd-CVD, complementary investigation of deposition conditions for nanocomposite **8** formation, TEM and EDX data for nanocomposite **8**, self-assembly and Pd-CVD of phosphine oxide **7**.

Acknowledgements

This work was supported by the ANR–DFG program (ANR-16-CE92-0037-01 and Schr 597/31-1, “Hybridiams”), by the CNRS, Université de Bourgogne, Conseil Régional de Bourgogne through the *plan d'actions régional pour l'innovation* (PARI) and the *fonds européen de développement regional* (FEDER) programs. The work in Giessen was supported in part (for M.A.G., O.M., J.E.P.D., and P.R.S.) by the US Department of Energy, Office of Science, Basic Energy Sciences, Materials Sciences and Engineering Division, under contract DE-AC02-76SF00515. M.A.G. was supported for mobility by the “Université franco-allemande/Deutsch-Französische Hochschule”. We thank the reviewers for constructive remarks.

References

[1] a) W. L. Noorduin, A. Grinthal, L. Mahadevan, J. Aizenberg, *Science* **2013**, 340, 832; b) G. M. Whitesides, B. Grzybowski, *Science* **2002**, 295, 2418; c) X. Yan, S. Li, T. R. Cook, X. Ji, Y. Yao, J. B. Pollock, Y. Shi, G. Yu, J. Li, F. Huang, P. J. Stang, *J. Am. Chem. Soc.* **2013**, 135, 14036; d) S. Shankar, R. Balgley, M. Lahav, S. R. Cohen, R. Popovitz-Biro, M. E. van der Boom, *J. Am. Chem. Soc.* **2015**, 137, 226; e) M. Altman, A. D. Shukla, T. Zubkov, G. Evmenenko, P. Dutta, M. E. van der Boom, *J. Am. Chem. Soc.* **2006**, 128, 7374; f) M. Altman, O. Zenkina, G. Evmenenko, P. Dutta, M. E. van der Boom, *J. Am. Chem. Soc.* **2008**, 130, 5040; g) S. Motoyama, R. Makiura, O. Sakata, H. Kitagawa, *J. Am. Chem. Soc.* **2011**, 133, 5640; h) R. Makiura, S. Motoyama, Y. Umemura, H. Yamanaka, O. Sakata, H. Kitagawa, *Nat. Mater* **2010**, 9, 565; i) M. Sadakiyo, T. Yamada, H. Kitagawa, *J. Am. Chem. Soc.* **2009**, 131, 9906.

[2] a) H. Liu, Y. Li, S. Xiao, H. Gan, T. Jiu, H. Li, L. Jiang, D. Zhu, D. Yu, B. Xiang, Y. Chen, *J. Am. Chem. Soc.* **2003**, 125, 10794; b) H. Liu, J. Xu, Y. Li, Y. Li, *Acc. Chem. Res.* **2010**, 43, 1496; c) J.-K. Lee, W.-K. Koh, W.-S. Chae, Y.-R. Kim, *Chem. Commun.* **2002**, 138; d) H.-B. Fu, J.-N. Yao, *J. Am. Chem. Soc.* **2001**, 123, 1434.

[3] a) J. Yang, F. Muckel, W. Baek, R. Fainblat, H. Chang, G. Bacher, T. Hyeon, *J. Am. Chem. Soc.* **2017**, 139, 6761; b) M. V. Kovalenko, L. Manna, A. Cabot, Z. Hens, D. V. Talapin, C. R. Kagan, V. I. Klimov, A. L. Rogach, P. Reiss, D. J. Milliron, P. Guyot-Sionnnest, G. Konstantatos, W. J. Parak, T. Hyeon, B. A. Korgel, C. B. Murray, W. Heiss, *ACS Nano* **2015**, 9, 1012; c) X. Peng, L. Manna, W. Yang, J. Wickham, E. Scher, A. Kadavanich, A. P. Alivisatos, *Nature* **2000**, 404, 59; d) C. B. Murray, D. J. Norris, M. G. Bawendi, *J. Am. Chem. Soc.* **1993**, 115, 8706; e) J. Chen, X. Zhao, S. J. R. Tan, H. Xu, B. Wu, B. Liu, D. Fu, W. Fu, D. Geng, Y. Liu, W. Liu, W. Tang, L. Li, W. Zhou, T.

C. Sum, K. P. Loh, *J. Am. Chem. Soc.* **2017**, 139, 1073; f) W. Chen, J. Zhao, J. Zhang, L. Gu, Z. Yang, X. Li, H. Yu, X. Zhu, R. Yang, D. Shi, X. Lin, J. Guo, X. Bai, G. Zhang, *J. Am. Chem. Soc.* **2015**, 137, 15632.

[4] a) G. Rogez, C. Massobrio, P. Rabu, M. Drillon, *Chem. Soc. Rev.* **2011**, 40, 1031; b) R. Costi, A. E. Saunders, U. Banin, *Angew. Chem. Int. Ed.* **2010**, 49, 4878; c) C. Zhu, S. Dong, *Nanoscale* **2013**, 5, 10765; d) A. Bétard, R. A. Fischer, *Chem. Rev.* **2012**, 112, 1055.

[5] a) S. Hermes, F. Schröder, R. Chelmowski, C. Wöll, R. A. Fischer, *J. Am. Chem. Soc.* **2005**, 127, 13744; b) O. Shekhah, H. Wang, S. Kowarik, F. Schreiber, M. Paulus, M. Tolan, C. Sternemann, F. Evers, D. Zacher, R. A. Fischer, C. Wöll, *J. Am. Chem. Soc.* **2007**, 129, 15118; c) A. Umemura, S. Diring, S. Furukawa, H. Uehara, T. Tsuruoka, S. Kitagawa, *J. Am. Chem. Soc.* **2011**, 133, 15506; d) J.-L. Zhuang, M. Kind, C. M. Grytz, F. Farr, M. Diefenbach, S. Tussupbayev, M. C. Holthausen, A. Terfort, *J. Am. Chem. Soc.* **2015**, 137, 8237.

[6] a) Y. Kim, J. Lee, M. S. Yeom, J. W. Shin, H. Kim, Y. Cui, J. W. Kysar, J. Hone, Y. Jung, S. Jeon, S. M. Han, *Nat. Commun.* **2013**, 4, 2114; b) X. Li, W. Cai, J. An, S. Kim, J. Nah, D. Yang, R. Piner, A. Velamakanni, I. Jung, E. Tutuc, S. K. Banerjee, L. Colombo, R. S. Ruoff, *Science* **2009**, 324, 1312.

[7] a) S. Cobo, G. Molnár, J. A. Real, A. Bousseksou, *Angew. Chem. Int. Ed.* **2006**, 45, 5786; b) K. Kanaizuka, R. Haruki, O. Sakata, M. Yoshimoto, Y. Akita, H. Kitagawa, *J. Am. Chem. Soc.* **2008**, 130, 15778.

[8] a) C. Xu, X. Wang, J. Zhu, *J. Phys. Chem. C* **2008**, 112, 19841; b) F.-X. Xiao, J. Miao, B. Liu, *J. Am. Chem. Soc.* **2014**, 136, 1559; c) B. F. Machado, P. Serp, *Catal. Sci. Technol.* **2012**, 2, 54; d) H. Wang, J. T. Robinson, G. Diankov, H. Dai, *J. Am. Chem. Soc.* **2010**, 132, 3270; e) H. Wang, H. S. Casalongue, Y. Liang, H. Dai, *J. Am. Chem.*

Soc. **2010**, 132, 7472; f) M. Jahan, Q. Bao, J.-X. Yang, K. P. Loh, *J. Am. Chem. Soc.* **2010**, 132, 14487.

[9] a) J. Kong, M. G. Chapline, H. Dai, *Adv. Mater.* **2001**, 13, 1384; b) V. Subramanian, E. E. Wolf, P. V. Kamat, *J. Am. Chem. Soc.* **2004**, 126, 4943; c) G. G. Wildgoose, C. E. Banks, R. G. Compton, *Small* **2006**, 2, 182; d) A. L. Balch, K. Winkler, *Chem. Rev.* **2016**, 116, 3812; e) S. Bhattacharya, S. K. Samanta, *Chem. Rev.* **2016**, 116, 11967; f) V. Georgakilas, J. N. Tiwari, K. C. Kemp, J. A. Perman, A. B. Bourlinos, K. S. Kim, R. Zboril, *Chem. Rev.* **2016**, 116, 5464.

[10] Y. Liang, M. Ozawa, A. Krueger, *ACS Nano* **2009**, 3, 2288.

[11] a) J. E. Dahl, S. G. Liu, R. M. K. Carlson, *Science* **2003**, 299, 96; b) H. Schwertfeger, A. A. Fokin, P. R. Schreiner, *Angew. Chem. Int. Ed.* **2008**, 47, 1022; c) M. A. Gunawan, J.-C. Hierso, D. Poinsot, A. A. Fokin, N. A. Fokina, B. A. Tkachenko, P. R. Schreiner, *New J. Chem.* **2014**, 38, 28.

[12] a) J. E. Dahl, J. M. Moldowan, K. E. Peters, G. E. Claypool, M. A. Rooney, G. E. Michael, M. R. Mello, M. L. Kohnen, *Nature* **1999**, 399, 54; b) J. E. P. Dahl, J. M. Moldowan, T. M. Peakman, J. C. Clardy, E. Lobkovsky, M. M. Olmstead, P. W. May, T. J. Davis, J. W. Steeds, K. E. Peters, A. Pepper, A. Ekuan, R. M. K. Carlson, *Angew. Chem. Int. Ed.* **2003**, 42, 2040.

[13] M. A. Gunawan, D. Poinsot, B. Domenichini, P. R. Schreiner, A. A. Fokin, J.-C. Hierso, in *Chemistry of Organo-Hybrids*, (Ed: B. C. Charleux, C.; Lacote, E.; Coperet, C.), John Wiley & Sons, Inc. **2014**, p. 69.

[14] P.-L. E. Chu, L.-Y. Wang, S. Khatua, A. B. Kolomeisky, S. Link, J. M. Tour, *ACS Nano* **2013**, 7, 35.

[15] N. A. Fokina, B. A. Tkachenko, A. Merz, M. Serafin, J. E. P. Dahl, R. M. K. Carlson, A. A. Fokin, P. R. Schreiner, *Eur. J. Org. Chem.* **2007**, 4738.

[16] a) G. C. McIntosh, M. Yoon, S. Berber, D. Tománek, *Phys. Rev. B* **2004**, 70, 045401; b) A. A. Fokin, P. R. Schreiner, *Mol. Phys.* **2009**, 107, 823.

[17] L. Landt, K. Klünder, J. E. Dahl, R. M. K. Carlson, T. Möller, C. Bostedt, *Phys. Rev. Lett.* **2009**, 103, 047402.

[18] a) W. L. Yang, J. D. Fabbri, T. M. Willey, J. R. I. Lee, J. E. Dahl, R. M. K. Carlson, P. R. Schreiner, A. A. Fokin, B. A. Tkachenko, N. A. Fokina, W. Meevasana, N. Mannella, K. Tanaka, X. J. Zhou, T. van Buuren, M. A. Kelly, Z. Hussain, N. A. Melosh, Z.-X. Shen, *Science* **2007**, 316, 1460; b) W. A. Clay, Z. Liu, W. Yang, J. D. Fabbri, J. E. Dahl, R. M. K. Carlson, Y. Sun, P. R. Schreiner, A. A. Fokin, B. A. Tkachenko, N. A. Fokina, P. A. Pianetta, N. Melosh, Z.-X. Shen, *Nano Lett.* **2009**, 9, 57; c) Y. Nakanishi, H. Omachi, N. A. Fokina, P. R. Schreiner, R. Kitaura, J. E. P. Dahl, R. M. K. Carlson, H. Shinohara, *Angew. Chem. Int. Ed.* **2015**, 54, 10802.

[19] a) H. Bai, C. Li, G. Shi, *Adv. Mater.* **2011**, 23, 1089; b) L. Dai, D. W. Chang, J.-B. Baek, W. Lu, *Small* **2012**, 8, 1130; c) D. Jariwala, V. K. Sangwan, L. J. Lauhon, T. J. Marks, M. C. Hersam, *Chem. Soc. Rev.* **2013**, 42, 2824.

[20] K. T. Narasimha, C. Ge, J. D. Fabbri, W. Clay, B. A. Tkachenko, A. A. Fokin, P. R. Schreiner, J. E. Dahl, R. M. K. Carlson, Z. X. Shen, N. A. Melosh, *Nat. Nanotechnol.* **2016**, 11, 267.

[21] F. H. Li, J. D. Fabbri, R. I. Yurchenko, A. N. Mileshkin, J. N. Hohman, H. Yan, H. Yuan, I. C. Tran, T. M. Willey, M. Bagge-Hansen, J. E. P. Dahl, R. M. K. Carlson, A. A. Fokin, P. R. Schreiner, Z.-X. Shen, N. A. Melosh, *Langmuir* **2013**, 29, 9790.

[22] T. Petit, H. A. Girard, A. Trouve, I. Batonneau-Gener, P. Bergonzo, J.-C. Arnault, *Nanoscale* **2013**, 5, 8958.

[23] a) A. B. Lysenko, G. A. Senchyk, J. Lincke, D. Lassig, A. A. Fokin, E. D. Butova, P. R. Schreiner, H. Krautscheid, K. V. Domasevitch, *Dalton Trans.* **2010**, 39, 4223; b) B. E. K.

Barth, B. A. Tkachenko, J. P. Eußner, P. R. Schreiner, S. Dehnen, *Organometallics* **2014**, 33, 1678.

[24] a) G. S. Girolami, J. A. Jensen, J. E. Gozum, D. M. Pollina, *MRS Proceedings* **1988**, 121; b) J.-C. Hierso, C. Satto, R. Feurer, P. Kalck, *Chem. Mater.* **1996**, 8, 2481; c) J.-C. Hierso, R. Feurer, P. Kalck, *Chem. Mater.* **2000**, 12, 390.

[25] M. A. Gunawan, D. Poinsot, B. Domenichini, C. Dirand, S. Chevalier, A. A. Fokin, P. R. Schreiner, J.-C. Hierso, *Nanoscale* **2015**, 7, 1956.

[26] a) T. Clark, T. Knox, H. Mackle, M. A. McKervey, J. J. Rooney, *J. Chem. Soc., Faraday Trans.* **1975**, 71, 2107; b) J. S. Chickos, W. E. A. Jr., *J. Phys. Chem. Ref. Data* **2002**, 31, 537.

[27] A. Binder, M. Seipenbusch, G. Kasper, *Chem. Vap. Deposition* **2011**, 17, 54.

[28] J.-C. Hierso, R. Feurer, P. Kalck, *Coord. Chem. Rev.* **1998**, 178–180, 1811.

[29] a) C. Dossi, R. Psaro, A. Bartsch, E. Brivio, A. Galasco, P. Losi, *Catal. Today* **1993**, 17, 527; b) A. Niklewski, T. Strunskus, G. Witte, C. Wöll, *Chem. Mater.* **2005**, 17, 861; c) C. Liang, W. Xia, H. Soltani-Ahmadi, O. Schluter, R. A. Fischer, M. Muhler, *Chem. Commun.* **2005**, 282; d) S. Hermes, M.-K. Schröter, R. Schmid, L. Khodeir, M. Muhler, A. Tissler, R. W. Fischer, R. A. Fischer, *Angew. Chem. Int. Ed.* **2005**, 44, 6237; e) Q. H. Wu, M. Gunia, T. Strunskus, G. Witte, M. Muhler, C. Wöll, *Chem. Vap. Deposition* **2005**, 11, 355; f) C. Liang, W. Xia, M. van den Berg, Y. Wang, H. Soltani-Ahmadi, O. Schlüter, R. A. Fischer, M. Muhler, *Chem. Mater.* **2009**, 21, 2360.

[30] a) C. P. Mehnert, D. W. Weaver, J. Y. Ying, *J. Am. Chem. Soc.* **1998**, 120, 12289; b) X. Mu, U. Bartmann, M. Guraya, G. W. Busser, U. Weckenmann, R. Fischer, M. Muhler, *Appl. Catal. A* **2003**, 248, 85.

[31] J. J. Senkevich, G. R. Yang, T. M. Lu, T. S. Cale, C. Jezewski, W. A. Lanford, *Chem. Vap. Deposition* **2002**, 8, 189.

[32] O. Moncea, M. A. Gunawan, D. Poinsot, H. Cattey, J. Becker, R. I. Yurchenko, E. D. Butova, H. Hausmann, M. Šekutor, A. A. Fokin, J.-C. Hierso, P. R. Schreiner, *J. Org. Chem.* **2016**, 81, 8759.

[33] a) G. A. Ten Eyck, J. J. Senkevich, F. Tang, D. Liu, S. Pimanpang, T. Karaback, G. C. Wang, T. M. Lu, C. Jezewski, W. A. Lanford, *Chem. Vap. Deposition* **2005**, 11, 60; b) J. W. Elam, A. Zinovev, C. Y. Han, H. H. Wang, U. Welp, J. N. Hryn, M. J. Pellin, *Thin Solid Films* **2006**, 515, 1664.

[34] XPS spectra include peaks labelled O KLL; these peaks represent the energy of the electrons ejected from the atoms due to the filling of the O 1s state (K shell) by an electron from the L shell coupled with the ejection of an electron from an L shell.

[35] J. F. S. Moulder, W. E.; Sobol, P. E.; Bomben, K. D., *Handbook of X-Ray Photoelectron Spectrospcopy*, Perkin-Elmer Corp.: Eden Prairie, **1992**.

[36] T. L. Barr, *J. Phys. Chem.* **1978**, 82, 1801.

[37] D. Briggs, Seah, M.P., *John Wiley & Sons* **1993**, 1

[38] V. I. Nefedov, Y. V. Salyn, I. I. Moiseev, A. P. Sadovskii, A. S. Berenbljum, A. G. Knizhnik, S. L. Mund, *Inorg. Chim. Acta* **1979**, 35, L343.

[39] R. Yerushalmi, J. C. Ho, Z. Fan, A. Javey, *Angew. Chem. Int. Ed.* **2008**, 47, 4440.

[40] Z. Karpiński, in *Advances in Catalysis*, Vol. 37 **1990**, p. 45.

[41] F. J. Ibañez, F. P. Zamborini, *J. Am. Chem. Soc.* **2008**, 130, 622.